Design of a Solar Panel Deployment and Tracking System for PocketQube Pico-Satellite

Daizong Li
COMAC Customer Service, Commercial Aircraft Corporation of China, Ltd.
100 Jiangchuan Road(E), Shanghai, 200241, China. +86 (0)2120875961
lidaizong@163.com

Patrick Harkness*
School of Engineering
University of Glasgow
James Watt Building South, Glasgow, G12 8QQ, UK. +44 (0)141 330 3233
Patrick.Harkness@glasgow.ac.uk

Tom Walkinshaw
Alba Orbital Ltd (PocketQube Shop)
5.13 The Whisky Bond,
2 Dawson Road, Glasgow, G4 9SS, UK.
+44 (0)845 689 0098
tom@pocketqubeshop.com

***Abstract*— Modularized small satellites will have even greater potential with better energy supply. In this paper, a PocketQube solar panel deployment and tracking system will be presented. The system is designed for a 3P PocketQubes. During the designing phase, trade-off analysis is done to meet the balance of weight, dimension and efficiency. Reliability, manufacturability, and cost are also considered from the beginning, as commercial production and launch are expected. The CAD design, dynamics analysis, motion simulation, and rendering for the project are undertaken by Solidworks, whereas Abaqus CAE is utilized for the finite element analysis of the vibration test of the panels. In the gimbal subsystem, we use two micro stepper motor to drive the panels via a two-axis gearbox, enabling the panels to track the sun omnidirectionally. In the panel subsystem, two types of customized spring hinges are designed. Robust and verified parts, such as burner resistors, are chose for the control and deployment system. After the continuous optimization process throughout the design phase, by comparing different manufacturing processes technologies, materials, and design details, the full scale prototypes of the gimbal subsystem were built and tested. In the end, the most feasible solution, as well as the suggestions for the development, were put forward.**

TABLE OF CONTENTS

1. INTRODUCTION 1
2. GENERAL DESIGN 2
3. DESIGN OF THE GIMBAL SUBSYSTEM 3
4. DESIGN OF THE PANEL SUBSYSTEM 9
5. DYNAMICS AND VIBRATION ANALYSIS 10
6. PROTOTYPING AND SUGGESTIONS 14
7. SUMMARY 17
REFERENCES 17
BIOGRAPHY 19

1. INTRODUCTION

Modularized small satellites attract considerable interest and have great potential. For Cubesats and PocketQubes as nanosatellites (1-10kg) and picosatellites (0.1-1kg), many space applications, say, data collection [1], earth observation [2], solar sail research [3], signal measurement [4], ship tracking [1], technical demonstration [5], and even asteroid exploration, etc, can be observed to prove their capacity with a low cost. Estimated by Alba Orbital, the cost of Pocketqube and Cubesat can be as low as around £22,000 and £99,000 respectively, including launching fee to LEO [6].

A typical 1P PocketQube is with a size of 5x5x5cm, and a weight of less than 200 grams. As shown in **Figure 1**, a 3P PocketQube skeleton have a size of 178mm x 50mm x 50mm external, and 178mm x 47mm x 47mm internal (widest point), weight 151g. While the volume and mass of a 3P PocketQube is still smaller than a 1U CubeSat, its shape enable it to take similar payload of a 1U CubeSat, saving space by using ¼ size standard PCB (40mm x 40mm) of that of CubeSat.

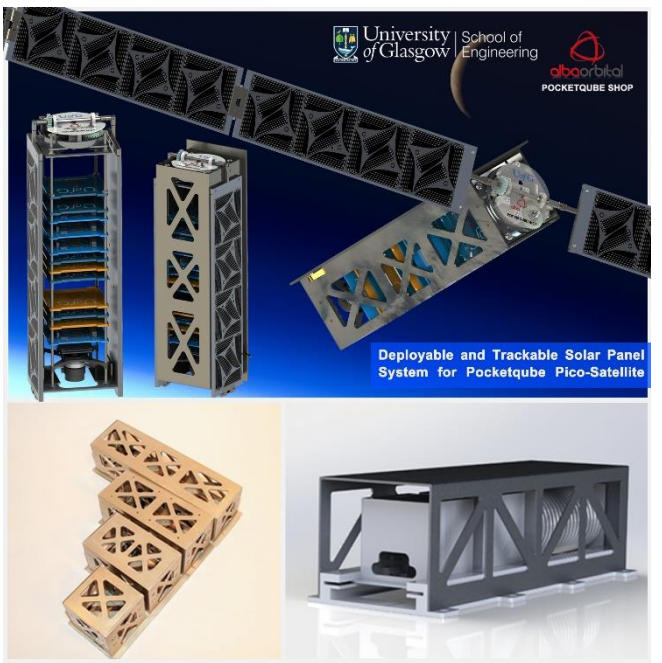

Figure 1. Top: Poster – 3P PQ & Solar Panel System Below Left: Photos- the 1P,1.5P,2P,3P PQ Skeletons Below Right: Illustration- PQ Launcher with a 2P PQ

However, energy problem is always an obstruction for operations of nanosatellites and picosatellites. The energy in the space is mainly generated by solar cells, and is very well determined by solar cells' efficiency and active area. For small satellite, the only currently practical option to increase energy supply is to mount more solar cells, which, however, is strictly limited by small satellite's size, mass, and payload. For PocketQube, currently there are only fixed solar panels available for adding on the external surface of the

*Corresponding author.

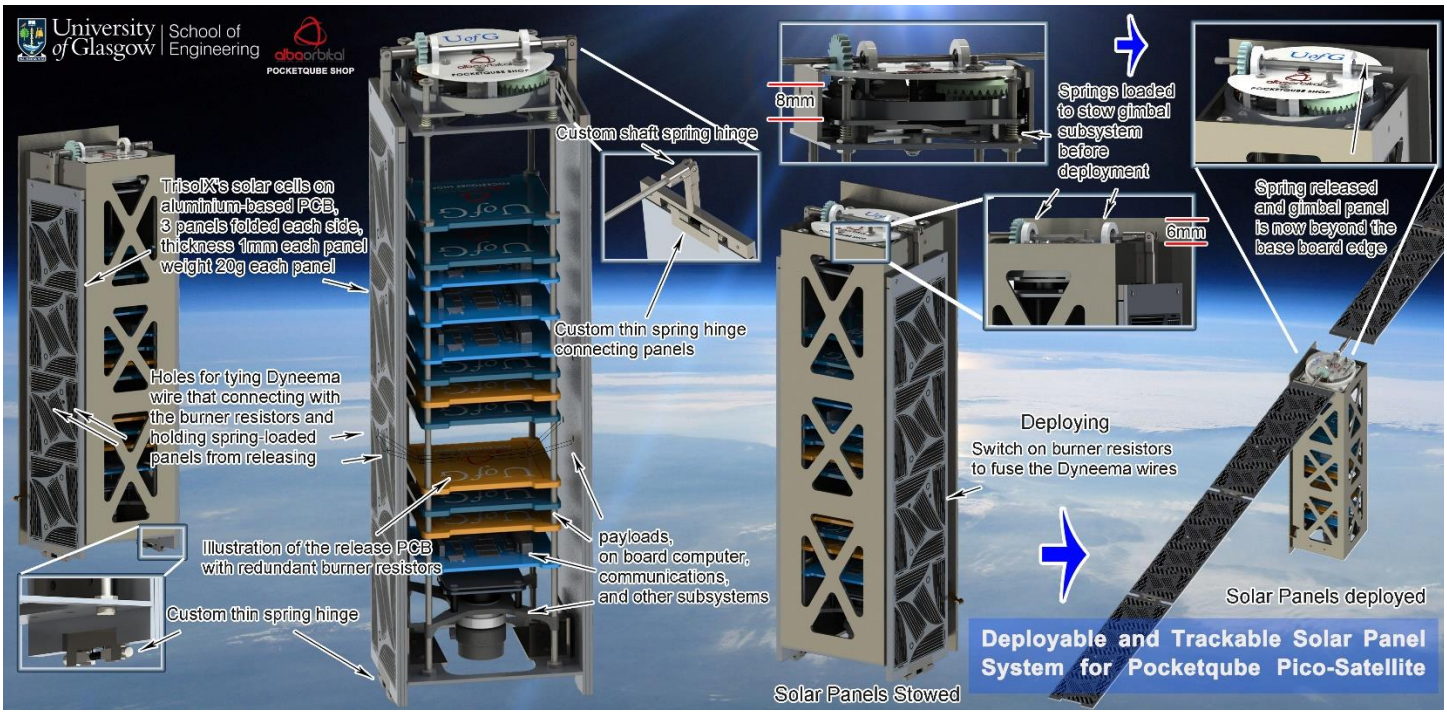

Figure 2. The System Structure and Deploying Process

PocketQube skeleton. For the bigger Cubesat, only fixed or deployable (but no tracking feature) solar panel systems are available in the market.

In order to enhance Pocketqube's energy supply, we aim to develop a deployable solar panel system that can track the sun omnidirectionally (**Figure 1**). Through this method, more solar cells can be mount on the small satellites, and more solar cells can be active concurrently.

2. General Design

2.1. Design Parameters and Requirement

The system mounts 6 deployable solar panels, and the mass is 168±5 grams for the ABS 3D printing edition, 182±5 grams for the CNC alloy edition.

Some parts is specified by Alba Orbital, say, the selection of solar cells (TrisolX Solar Wings). For each TrisolX solar cell, with 1 sun, AM 1.5G (100mv/cm^2), 25°C, max power is 34mW, efficient is 28%. For each system, we mount 144 TrisolX solar wings (For the design of solar panels, please refer to section 4.1). Therefore, the max power of the system is 4.9W, and overall power-weight ratio of the micro solar array, deployment and solar tracking system is about 26.9 Watt/kg (1 sun, AM 1.5G (100mv/cm^2), 25°C).

Using feasible and verified technologies in this project is important. Reliability, manufacturability, and cost are also considered from the beginning, as commercial production and launch are expected. A compact design is needed to maximum the payload capacity.

Comparing to the add-on fixed solar panels method, by using the same type of solar cells, the deployable system can generate around 4 times more energy.

2.2. The System Structure

As shown in **Figure 1** (below right), before the PocketQube satellite is released in space by rocket or other spacecraft (eg. ISS, space shuttle, other satellites), it will be fixed in a PocketQube launcher. A 192x56x1.6mm base plate and two kill switches (**Figure 2**) are used, fastening PocketQube in the launcher. The distance between the edge of the base plate and the skeleton is 6mm each side on long edge and 3mm on short edge. The base plate acting as a track when the PocketQube is being released by the launcher.

While fixed in the launcher at the stowed mode (**Figure 2**), the spring-loaded panels are holded from deploying by the Dyneema wire that connected with burner resistors and tired with the panels on the release holes. These release holes are arranged on the same position (while folded) on the three layers of the panels each side.

TrisolX's wing-shape solar cells are installed on the aluminium-based PCB, 3 panels folded each side. For each panel, the thickness is 1mm while the weight is around 20g. Aluminium-based PCB was chose here because of its higher strength comparing with the FR4 glass-reinforced epoxy laminate sheets. While its price is at an acceptable range, as about 1.5 times higher than FR4 PCBs. The panels are loaded by three customized spring hinges each side.

2.3. The Deploying Process

As shown in **Figure 2,** inside the satellite, the payloads and PCBs are installed on the 180mm M2 threaded rod and separated by the threaded stands. For the releasing board and burner resistor circuit design, we use the same system with the previous AEOLDOS project presented by Patrick Harkness from University of Glasgow [3].

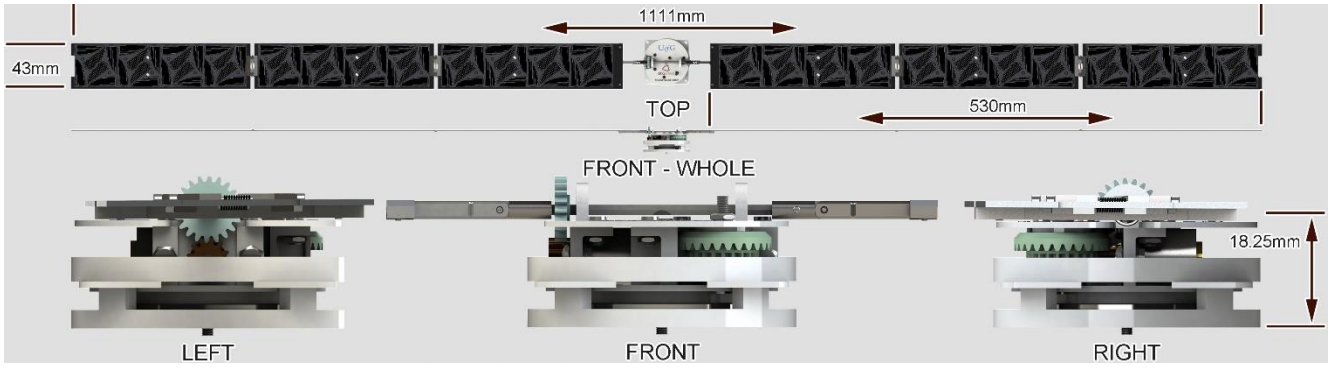

Figure 3 The Dimension of the Solar Panels

During the deploying process, by the switching on the burner resistors, the Dyneema wires will be fused, releasing the spring-loaded solar panels. On the release PCB, redundant burner resistors and circuit is set to ensure the reliability, while a set of sensors is also suggested to be add to check the status of the deploying processing.

As mentioned above, there is a 6mm margin from the edge of the base plate on the top of PocketQubes (**Figure 2 Right**), which will block the gimbal from freely rotating. To solve this problem, as shown in **Figure 2 Right**, we use four compression springs on the rod to enable the gimbal being stowed before the deployment, and being ejected by the springs after the deployment to ensure the panels can 360-degree freely rotate.

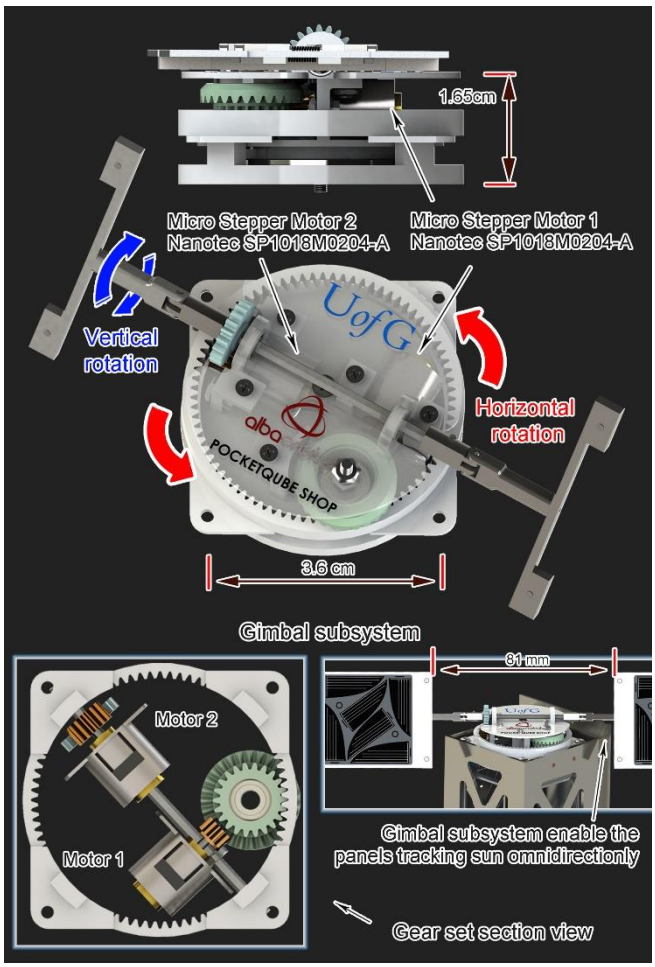

Figure 4. The Gimbal Subsystem and Solar Tracking

2.4. The Solar Tracking

A two-axis gimbal subsystem is needed to realize the solar tracking function for the solar panels, enabling a 360 degree pointing capacity. After mechanical calculation, two stepper motors were selected in the trade-off process from a comparison of stepper motor, servomotor, and ultrasonic motor, and a further comparison from five micro stepper motors of three manufacturers.

Based on the calculated result and the selected motor, as shown in **Figure 4**, a planetary crown-spur double gear is designed to mesh with a ring-type internal gear and to compress the gearbox's size and thickness, allowing to install both motors by a parallel layout inside the gearbox. This layout of motors is better than a layout that motor 2 rotating with gimbal while motor 1 fixed with the satellite, as by installing the motors inside the gearbox, this layout not only can further compact the gimbal, but can simplify the arrangement of wires.

3. Design of the Gimbal Subsystem

3.1. Mechanical Analysis

We need to analysis the required torque of the gimbal for the solar tracking function. As shown in **Figure 4**, the overall length of the deployed six panels is 1111mm, the width is 43mm, and the thickness of the panels is 1mm. For the weight, by isolating the corresponding parts and by applying the corresponding materials in the Solidworks software by "mass properties" analysis, we can measure that the total mass of the solar panels, hinges, shaft, and shaft gear is 113.56 grams. Considering different materials and parts may be utilized, we then use 120 grams calculating the rotational inertia.

This light mass property is partly benefit from the light weight design, say, the 1mm thickness aluminium alloy PCB substrate of the panel to balance the light weight, strength and

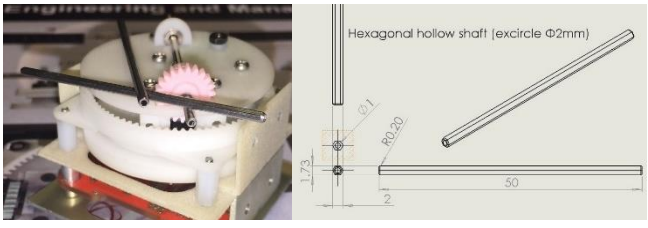

Figure 5. The Hexagonal Hollow Shaft Can Achieve the Required Strength with a Lightest Mass

torsion resistance; As shown in **Figure 5**, similar example can be seen as the hexagonal hollow shaft.

Recall from Dynamics, for a constant shape of body, the moment of inertia appears I in Newton's law of motion as the ratio of an applied torqueτon it to the angular acceleration α around a principal axis, as: $\tau = I \times \alpha$; [7]

Whereas, for the moment of inertia:

$$I = \int_m r^2 dm = \sum_{i=1}^{N} m_i r_i^2 ;$$

For Solid cuboid of height h, width w, and depth d, and mass m,

$$\begin{cases} I_h = \frac{m(d^2+w^2)}{12} \\ I_w = \frac{m(h^2+d^2)}{12}; [7] \\ I_d = \frac{m(h^2+w^2)}{12} \end{cases}$$

3.1.1. Vertical Rotation

As shown in **Figure 4**, the gimbal's horizontal and vertical rotation were named. For the moment of inertia for the vertical rotation:

$$I_v = \frac{m(h^2+d^2)}{12} = \frac{0.12kg \times (0.043^2 + 0.001^2)}{12} = 0.0000185 \text{kg} \cdot \text{m}^2;$$

Considering the PocketQube satellite is on a 90 minutes orbital period Low Earth Orbit, ignoring the earth revolution, the minimum revolving speed to track the sun is: (1/90) revolution per minute (0.01111rpm). In this case, we set the reference revolving speed of both the vertical and horizontal rotation as ω = 1 rpm = 0.1047 rad/sec. Assuming we need the gimbal reach this speed in 1 second, the angular acceleration α = ω/t = 0.1047rad/s^2. Therefore, the required torque on vertical rotation is:

$$\tau_v = I_v \times \alpha = 0.0019 \text{ mNm}.$$

3.1.2. Horizontal Rotation

For thin rectangular plate of height h and of width w and mass m, when the axis of rotation perpendicular to the plate at the centre of gravity, $I = \frac{m(h^2+w^2)}{12}$; [7]

Noting that when the panels are parallel to horizon plane, its horizontal rotation's moment of inertia reaching the maximum. Therefore, for the panels, hinges, shaft, and shaft gear, the horizontal rotation's moment of inertia is:

$$I_{h1} = \frac{0.12kg \times (1.111^2 + 0.043^2)}{12} = 0.0124 \text{ kg} \cdot \text{m}^2;$$

For the horizontal rotating parts of the gimbal subsystem (**Figure 6**), including the top board, motor board, step motors,

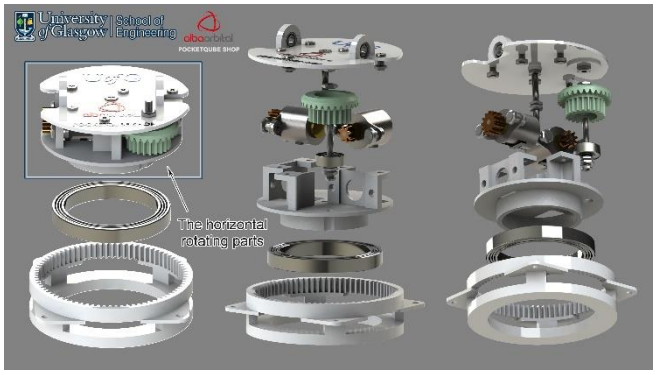

Figure 6. The Gimbal's Horizontal Rotating Parts and the Explosive View

gear set (exclude the shaft gear, and the internal gear structure), bearings (exclude the Ø32mm ring-type bearing), and the screws/nuts, the total mass of them is 16.78 grams (the 3D-printing photosensitive resin edition). By applying the aluminium alloy's material property to the top board and motor board, we can gain the corresponding mass for the CNC-processing aluminium alloy version is 23.01 grams. Considering the possible weight of the wires and other components, we set 25 grams for calculation.

Assuming the above-mentioned horizontal rotating parts as one solid density-even-distributed cylinder, the radius is 21.5 mm. For cylinder, $I = \frac{mr^2}{2}$; [7]

Therefore, for the gimbal's horizontal rotating parts, moment of inertia is:

$$I_{h2} = \frac{0.025kg \times (0.021m)^2}{2} = 0.0000056 \text{ kg} \cdot \text{m}^2;$$

Similar to the vertical rotation, the angular acceleration α = ω/t = 0.1047rad/s^2; Therefore, the required torque on gimbal's horizontal rotation is:

$$\tau_h = (I_{h1} + I_{h2}) \times \alpha = 1.30 \text{ mNm}.$$

3.2. Selection of Motors

3.2.1. Tread-off of Stepper Motors and Servo Motors

Stepper motor, servomotor, and ultrasonic motor from several suppliers are compared to select the most matched motor for creating a compact, reliably, and cost efficient design.

Stepper motors and servo motors are well proven technologies, and many suppliers can be easily found and compared. Servo motors and Stepper motors from Micromo (FAULHABER), Nanotec, and Portescap are studied, the size of micro stepper motors are correspondingly smaller. For same diameter and torque motors, the length of servomotors are notably longer than corresponding stepper motors, as the stepper motor do not have integrated encoders on it.

Step angle of micro stepper motors ranges from 15 Degree to 24 Degrees, whereas the step resolution of servo motors are decided by the encoders it combined with, which can be much precise, for example, for Micromo DC-Servomotors 0824B

Figure 7. Ring-type Ultrasonic Motor [11] [12]

[8], the range of the resolution could be 4096 lines (with the Encoders Series AESM-4096, 0.088 degree of step resolution). However, if we have an enough reduction ratio offered by the gearbox, the stepper motor's step angle is enough for the panels' tracking. On the other hand, closed-loop stepper motor's positioning accuracy of stepper motors is far behind that of open-loop servomotor [9], for example, Nanotec's SP1018M have a step accuracy of 7% [10]. While its step angle is 18 degrees, SP1018M's step accuracy is 1.26 degree. However, such accuracy of step motor is non-accumulative, which means such stepper motor's positioning accuracy is enough for our design.

What's more, stepper motor's controller board is easier to develop and integrate than the servo motor. That is important because all of the provided controller for the stepper motors or servomotors from Micromo, Nanotec, and Portescap, are too big for the ProcketQube. We can build a control PCB much easier for steppers, and integrating the control of both the two motors into one PCB can further save the limited onboard space. Finally, the cost is also an important factor. Stepper motors were long considered as the cost effective alternative for applications that do not require the high performance of servomotors [9].

3.2.2. Tread-off of Stepper Motors and Ultrasonic Motors

Ring-type ultrasonic motor (USM, also refer to ring piezoelectric motor), have already been used on high-end SLR camera lens by Canon for more than 30 years (**Figure 7**) [11], is driven by ultrasonic vibrations created from the piezoelectric material used in the motor.

Being ring-shaped, Ring-type USM ideally suits to not only the shape of a SLR lens barrel, but also our gimbal system's size. It has advantages such as high torque at low rotate speed and high torque-to-mass ratio [12], and most important, is very thin and compact. It can directly drive the system without gears, saving space dramatically for the system. In addition, ring-type USM is also highly efficient featured with low power consumption, having a high holding torque when they are inactive, and generating no magnetic interference [13]. USM's rotating speed is highly controllable, as it has the micrometer level control precision. Also, USM is stable across a wide range of temperatures, the TRUM-30A ultrasonic motor [14] equipped by Chang'e 3 lunar lander have a working temperature of -120°C to 180°C.

The above-mentioned advantages make USM quite suitable for applications in space. A Lithuanian CubeSats (LitSat-1) was deployed in 2014 from International Space Station to test an onboard Piezoelectric Reaction Sphere [5]. Another example can be seen as the Transusm's TRUM-30A ultrasonic motor [14] that equipped by China's Chang'e 3 lunar lander's infrared imaging spectrometer, was verified in 2013.

But as the commercial suppliers of ultrasonic motors are very rare, the price is normally much higher than the steppers, say, a space-verified ultrasonic motor is normally higher than £300 each [14] [15], although that price can normally covered a Canon's SLR lens equipped with Ring-type USM motor. Another limitation can be seen as the control of ultrasonic motors is harder to develop, as high frequency and voltage is needed to drive the USM. What's more, while we need two motors to drive two axis rotation, only one USM is needed for the horizontal motion, which leads to a complex motor control system, as integrating the control system of one USM and one stepper in one 40mm*40mm PocketQube sized PCB is more complicated than simply integrating that of two stepper motors.

However, inspired by the Ring-shape structure, we come up with the solution that applying ring-type internal gear and crown gear to compress the gearbox's size and thickness. In this way, by considering the high cost and complexity raised by ultrasonic motors, the stepper motors is more suitable for our project.

3.2.3. Selection of Micro Stepper Motor

As shown in **Table 1**, five micro stepper motor models were selected comparison: Micromo's FDM0620 [16], Micromo's

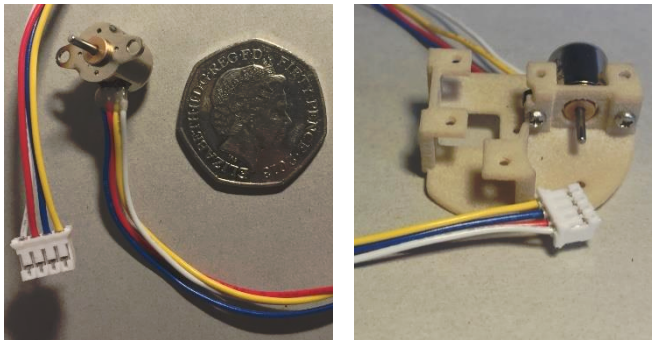

Figure 8. Left: Nanotec SP1018M / 50p coin
Right: Nanotec SP1018M Mount on Gearbox

Table 1 Comparison between Selected Micro Stepper Motors [16] [17] [10] [18] [19]

Specification	SP1018M	P010 064	P010 104	AM0820	FDM0620
Manufacturer	**Nanotec**	Portescap	Portescap	Micromo	Micromo
Voltage per phase at both phases on, V	**3.3**	2.20	2.20	3	3
Current per phase at both phases on, A	**0.22**	0.15	0.15	0.15	0.08
Phase resistance, Ω	**15±7% (25°C)**	19	19	18	30
Phase inductance, mH	**3.0 (1KHz)**	13.7	13.7	3.9	4.5
Holding torque, mNm	**1.6**	1.8	1.5	0.65	0.25
		2.5 (1.5x current)	2.1 (1.5x current)		
				1 (2x current)	0.39 (2x current)
Detent torque, mNm	**0.048**	0.04	0.04	0.17	0.06
Step angle, deg	**18**	15	9	18	18
Steps per revolution	**20**	24	40	20	20
Step accuracy	**±7%**	±5%	±5%	±10%	±5%
Rotor Inertia, kg-m^2	**1.0*10e-9**	7*10e-9	7*10e-9	2.75*10e-9	0.5*10e-9
Weight, g	**4.3**	9	9	3.3	1.1
Ambient temperature	**-20 ~ +50°C**	-20 ~ +50°C	-20 ~ +50°C	-30 ~ +70°C	-35 ~ +70°C
Diameter, mm	**Ø10.5**	Ø10	Ø10	Ø8	Ø6
Length (motor barrel only), mm	**10**	16.4	16.4	13.8	9.5

AM0820 [17], Nanotec's SP1018M0204-A (**Figure 8**) [10], Portescap's P010-064 [18], and Portescap's P010-104 [19].

Although Micromo FDM0620 is the smallest micro stepper motor that can fit our requirement, however, its price ($198.98 each without matched gearbox [16]) is much higher than the Nanotec's SP1018M (€22.6 each) [10]. Adding the fact that Nanotec SP1018M is the one with the highest torque-to-size ratio and torque-to-weight ratio, Nanotec SP1018M is finally chose for the gimbal subsystem (**Figure 8**).

While all of these three companies' have their stepper motors space verified, the ambient temperature range of SP1018M is -20°C to +50°C, which is same to that of Portescap's P010-064, yet smaller than FDM0620's -35°C to +70°C. However, Nanotec offer custom options such as High-Temperature Winding and Seals adapting high and low temperatures and vacuum [20]. Therefore, we can extend SP1018M's ambient temperature when it is necessary.

3.3. Gear Set Design

3.3.1. Gearbox Layout, Drive Ratio, and Drive Efficiency

Nanotec SP1018M stepper motor (**Figure 8**) is selected for the gimbal design. Its holding torque at nominal current is 1.6 mNm, and its step angle is 18 degree (**Table 1**).

Recall that from section 3.1, the required gimbal torque are: vertical $\tau_v = 0.0019$ mNm; horizontal $\tau_h = 1.30$ mNm. It should be noted that these two torque is without the consideration of friction. However, by using bearing on all rotating joints (**Figure 9**), the frictions will be reduced dramatically. Moreover, since the motor's 1.6 mNm holding torque is at the nominal current only, as at low speed stepper motor typically have an around 1.5x torque with 2x current, we can be certain that the even only use the motors themselves without the reduction gear set, the torque is enough to drive the gimbal.

However, a gear set is still needed for three reason: driving the gimbal's rotation, enabling a parallel layout of the two motors to reduce the thickness, and reducing the step angle.

As shown in **Figure 9**, we apply a planetary *crown-spur double gear* to mesh with the ring-type *internal gear* and to compress the gearbox's size and thickness, also, installing both of the motors by a parallel layout on the rotational part. This layout of motors can further compacting the gimbal, and simplifying the arrangement of wires.

For the horizontal rotation, the 8-tooth *pinion gear 1* is mounted on the shaft of *motor 1*, driving the 28-tooth crown gear part of the *crown-spur double gear* (28T-22T). Simultaneously, the 22-tooth spur gear part of the *crown-spur double gear* (28T-22T) is meshing with the 80-tooth internal gear structure. For the vertical rotation, a 22-tooth *spur gear* is directly derived by the 10-tooth pinion gear 2 on motor 2 (**Figure 9**). Therefore, the drive ratio of horizontal and vertical rotation are [21]:

$$\mathrm{R}_h = \frac{T_1}{T_2} \times \frac{T_3}{T_4} = \frac{8}{28} \times \frac{22}{80} = 1{:}\,12.73$$

$$\mathrm{R}_v = \frac{T_1}{T_2} = \frac{10}{22} = 1{:}\,2.2;$$

For one stage spur gears, while normal ratio range from 1:1 to 6:1 and pitch line velocity is less than 25m/s, gear drive efficiency is range from 98-99% [21]. Here we use the minimum 98% for calculation. The efficiency of a gear system is calculated as:

$$(\text{Output shaft power} \,/\, \text{Input shaft power}) \times 100\ \%;$$

Therefore, as the SP1018M motor's holding torque at the nominal current is 1.6 mNm, the output torque of horizontal and vertical rotation are:

$$\tau_{h\prime} = \tau_1 \times 12.73 \times 98\% \times 98\% = \mathbf{19.56\ mNm};$$

$$\tau_{v\prime} = \tau_2 \times 2.2 \times 98\% = 2.16\tau_2 = \mathbf{3.45\ mNm};$$

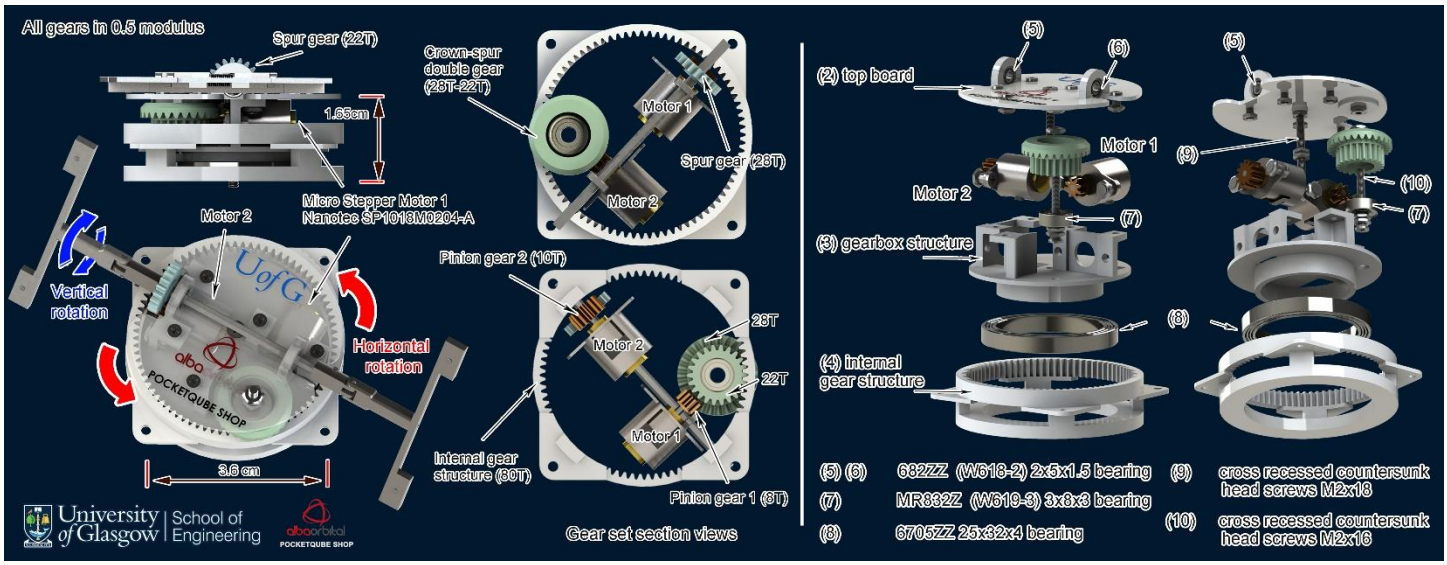

Figure 9. Left: Layout of Gear Set and Motors; Right: Layout of Bearings and Screws

The output step angle (full step) are:

$$\text{Horizontal rotation: } 18°/\,R_h = \frac{18°}{12.73} = 1.414°$$

$$\text{Vertical rotation: } 18°/\,R_v = \frac{18°}{2.2} = 8.18°$$

The output step angle (half step) are:

$$\text{Horizontal rotation: } 9°/\,R_h = 0.707°$$

$$\text{Vertical rotation: } 9°/\,R_v = 4.09°$$

Noting that for stepper motor, the half step mode contributes approximately 15%– 30% [22] less torque than the dual-phase full step mode.

The output step angle (8 microsteps) are:

$$\text{Horizontal rotation: } 2.25°/\,R_h = 0.177°$$

$$\text{Vertical rotation: } 2.25°/\,R_v = 1.023°$$

From Micromo's whire paper "Microstepping: Myths and Realities", we can notice that for two-phase stepper motors (including the selected SP1018M), while Microstepping can reduce the mechanical noise and reduce resonances problems, the incremental torque per microstep drops off dramatically [22]. For an 8 microstepping mode, the out torque is 19.51% of the full-step torque. Therefore, if we apply the 8 microstepping mode, the output torque will become around $\tau_{h''} = 3.81$ mNm and $\tau_{v''} = 0.67$ mNm. While they are notably lower than the output torque of full step mode as $\tau_{h'} = \mathbf{19.56\ mNm}$ and $\tau_{v'} = \mathbf{3.45\ mNm}$, they are still enough for the required $\tau_h = 1.3$mNm, $\tau_v = 0.0019$mNm we calculated from the section 3.1.

3.3.2. Gear Set Design

As shown in **Figure 11**, to positioning the motors, integrated design of the internal gear and the spur part of the planetary gear is firstly undertook, by the softwares Geartrax and Solidworks. By doing this, we determine to use Modulus 0.5 for all of the gears for the project.

After this, we then design the crown gear part of the double planetary gear. We choose crown gear rather than bevel gear to change the rotation direction is because crown gear is more compact and thin. To reduce friction of the plastic planetary double gear, a bearing is mounted on it (**Figure 10**).

Also to reduce thickness, the smallest 0.5 Mod pinion gear on market, with 8 teeth, is selected. Noting that the gearbox's space is very limited, therefore the motors' shaft need to be cut from 7.5 mm to 5.5 mm to meet the design, also, we need the pinion to be thinner than normal. Since the two pinions' teeth number are both less than 17, they need to be the profile shifted gear, or using generating cutting to cut a small profile at the teeth's root, to avoid undercutting [21]. Considering them, we decide to use an 8-tooth semi-custom pinion gear with 2.5mm height and Ø1.5mm inner diameter, the pinion is made by copper and using generating cutting process. Similarly, for the vertical rotation, a 10-tooth pinion gear with same height (2.5mm), inner diameter (Ø1.5mm), and

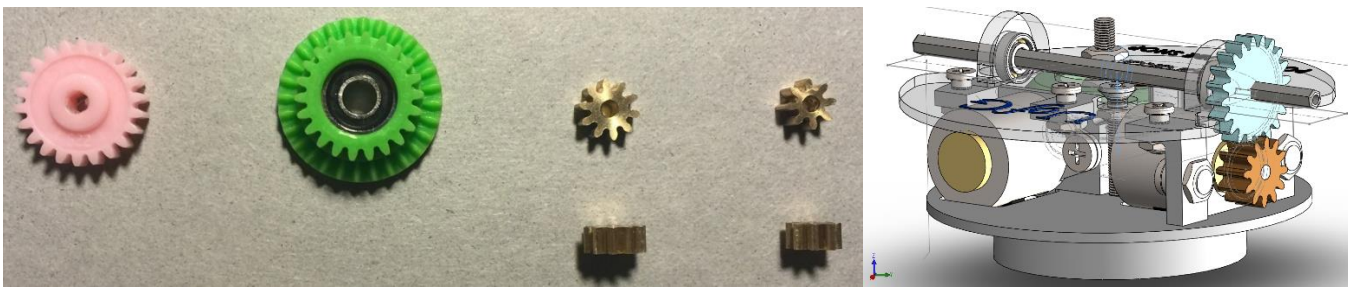

Figure 10. 22-Tooth Spur Gear, Crown-Spur Double Gear (28T-22T), 10-Tooth Pinion Gear 2, 8-Tooth Pinion

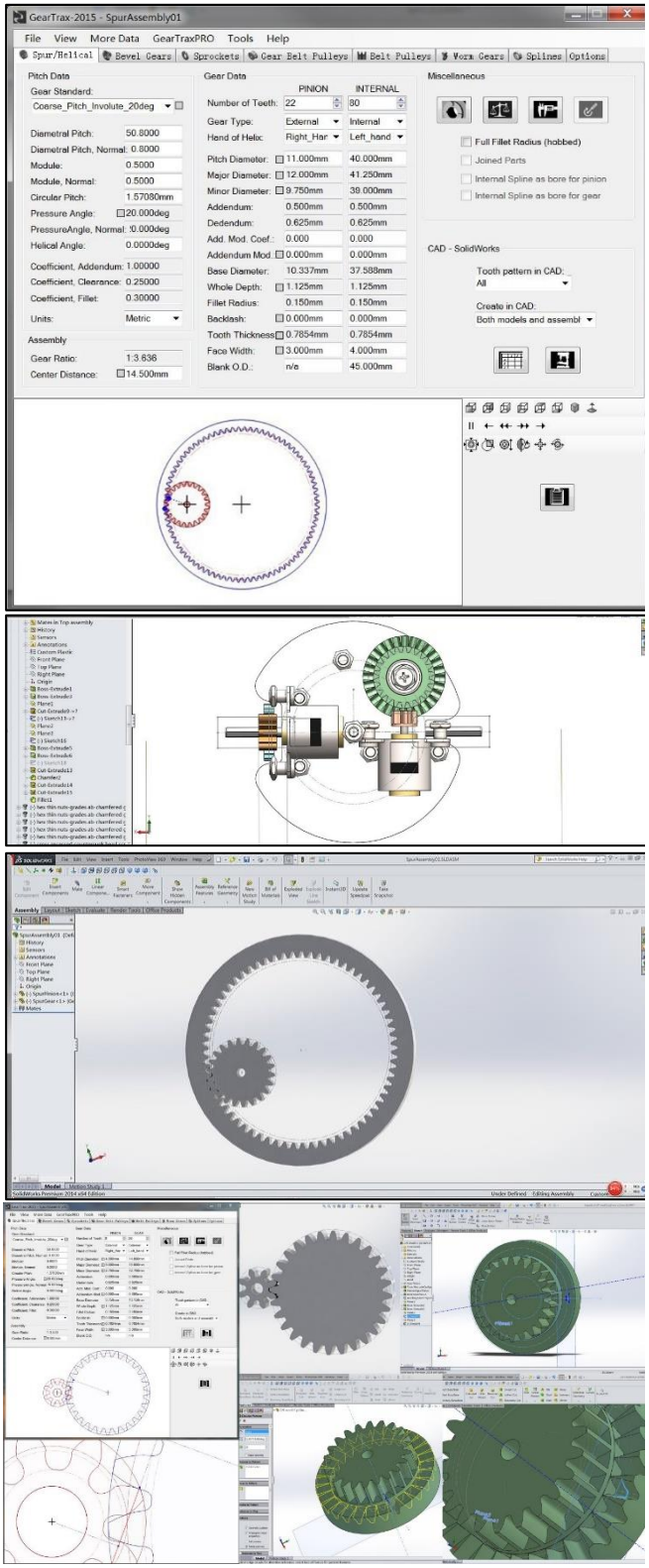

Figure 11. Design Process of the Gear Set

material (copper), is used to mesh with a 22-tooth plastic spur gear directly (**Figure 10**).

3.4. Gearbox Structure Design

Parts of the Gimbal structure are listed in **Figure 9**. As shown before in **Figure 5**, Main shaft (part (1)) is made by stainless steel (AISI 304). The hexagonal shape is applied, which

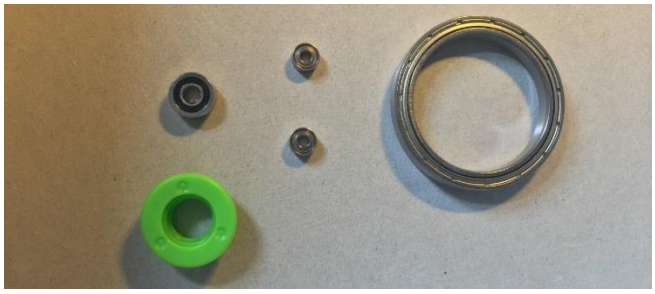

Figure 12. The Bearings on the Gimbal Subsystem

makes it easier for the torque transmission and assembly between the shaft and the gear. A hollow design can reduce the mass of the shaft while maintain the similar performance.

As shown in **Figure 9**, in the gearbox, except four M2.2x5 motor screws and nuts, all other screws are in M2 diameter. We use five M2x5 cross recessed cheese/round head screws, one M2x16 and one M2x18 cross recessed countersunk head screws. Correspondingly, two countersinks are used: one is for the middle hole on the part (2): top board (CNC processing aluminium alloy), one is the hole to install the planetary double gear from the part (3): gearbox structure (3D printing).

On the other hand, four bearings are utilized, two on the shaft, one in the planetary double gear, and one as the rotational connector of the gimbal itself (**Figure 9**, **Figure 12**). The model of bearings are:

Part (5) (6) 682ZZ (or SKF's W618-2) 2x5x1.5 mm Bearing;
Part (7) MR832Z (or SKF's W619-3) 3x8x3 mm Bearing;
Part (8) 6705ZZ 25x32x4 mm Thin Wall Deep Groove Ball Bearings.

Noted that for the Ring-type bearing (8), on the prototype, we use **Interference Fit** to connect the gimbal's rotational and fixed parts, however, for the future formal production, two fastening screws (setscrews), or space-verified adhesive, are

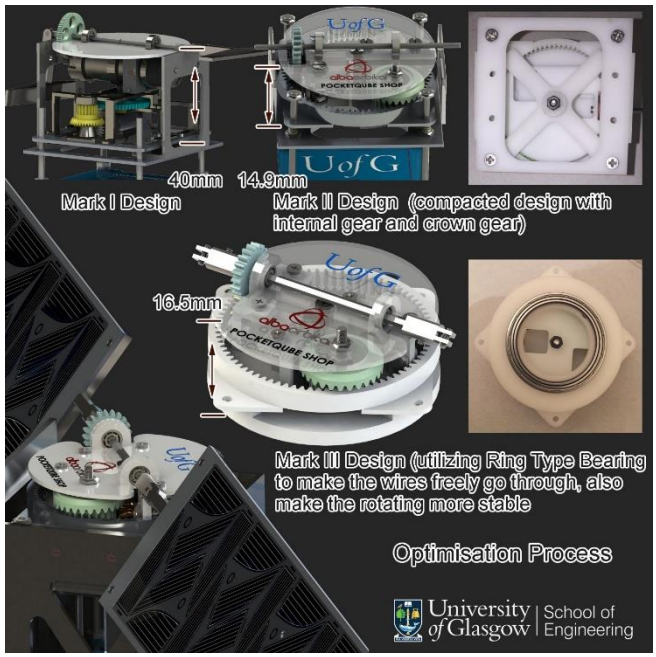

Figure 13. Illustration of Key Optimization Process

also needed to ensure the reliability of the connection to the ring bearing from part (3) and part (4).

3.5. Optimization Design

Optimisation designs are applied to continuously to improve the performance. Apart from the continuous optimising process in details throughout the project, we conduct two significant updating:

Firstly, as shown in **Figure 13,** using internal gear and a custom double crown-spur gear to compress the dimension of the gearbox design from a thickness of more than 40mm to less than 20mm. However, the problem of wiring is still exist, increasing the risk that the gimbal may get stuck by the wires of the stepper motors and solar panels. Another issue is that the holding nut cannot be totally locked, as that will also lock the gimbal. A negative effect from this issue is that an unstable rotation can be easily noticed on the prototype. A serious resonance can be expected even without the vibration test.

Secondly, to solve this problem, by utilizing ring type bearing, we make the wires of the motors and solar panels freely go through the gimbal, enhancing the stability of the gimbal's rotary motion in the meantime. On the prototype, this method makes the gimbal rotating significantly more stable.

4. DESIGN OF THE PANEL SUBSYSTEM

4.1. Solar Panels

TrisolX Solar Wings [23] (**Figure 14 above**) are required to use as solar cells for the project by Alba Orbital Ltd, and a possible layout of TrisolX wings (**Figure 14 middle**) were also provided. By comparing several possible layouts (**Figure 14**), we can gain the result that this layout is one of the most efficient layout of TrisolX wings on the 160x40mm panel. Please refer to section 2.1 for solar cell parameters.

TrisolX's wing are installed on the aluminium-based PCB, as aluminium-based PCB has a higher strength comparing with the FR4 glass-reinforced epoxy laminate sheets, while its price is at an acceptable range, as less than 1.5 times higher than FR4 PCBs (**Table 2**).

Table 2. Comparison of the cost between Aluminium and FR4 PCBs (leading time: 9days).

Quantity:	6	60	100	120
Material:				
Aluminium	£112.78	£188.66		£255.42
FR4	£112.39	£155.04	£183.67	

As shown in **Figure 15**, by arranging the distance between the panels from two sides, a distance of 81mm is set to avoid collision between the panels and skeleton. Therefore, the distance between the edge of the panel to the middle of the top board [part (2)] is 40.5mm. while the size of panel 1 (left side, right side identical) is 173x43mm, the panel 2 and panel

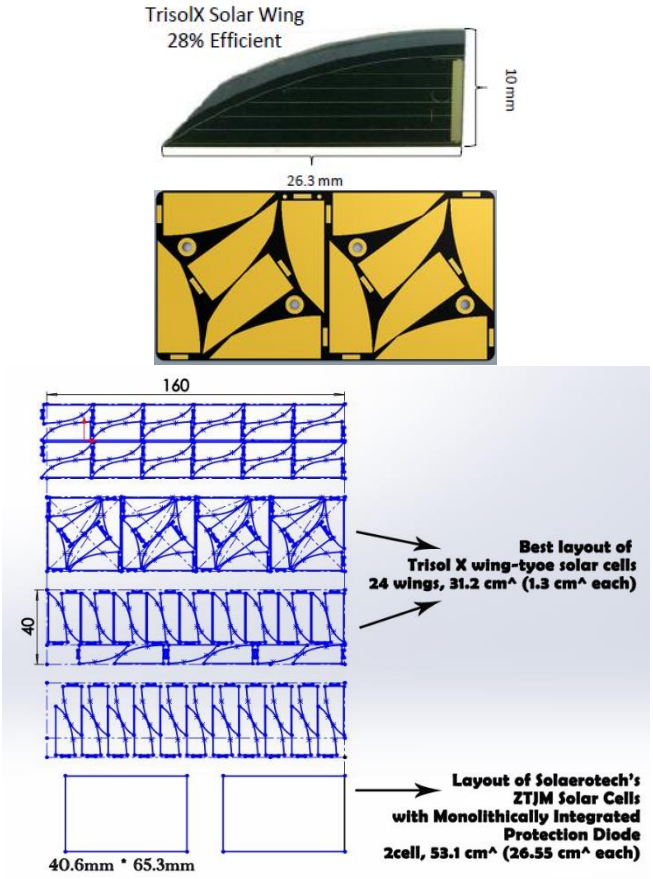

Figure 14. TrisolX-Solar-Wing (above) and Possible Layout of TrisolX Wings; source: Alba Orbital.

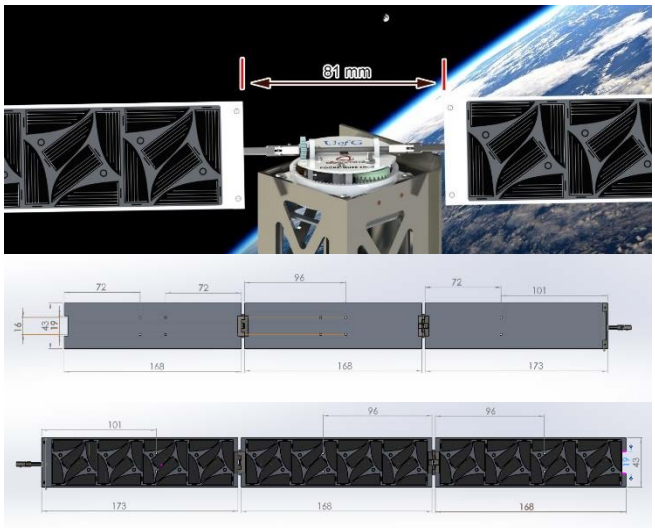

Figure 15. The Dimension of the Solar Panels

3 is identical (left side, right side still identical) with a size of 168x43mm. The distance from the releasing hole to the closer edge of each panels is 72mm. Noted that for the panel 2 and panel 3, they need to set four symmetrical releasing holes, as well as the whole panel, to be symmetrical, enabling a good compatibility of panel 2 and 3, to reduce the cost and complexity. On the other hand, two Countersink holes is needed on panel1, as M1x3 Countersunk head screws connect the panel 1 to the shaft spring hinge.

Figure 16. Four Screws on the Shaft Spring Hinge

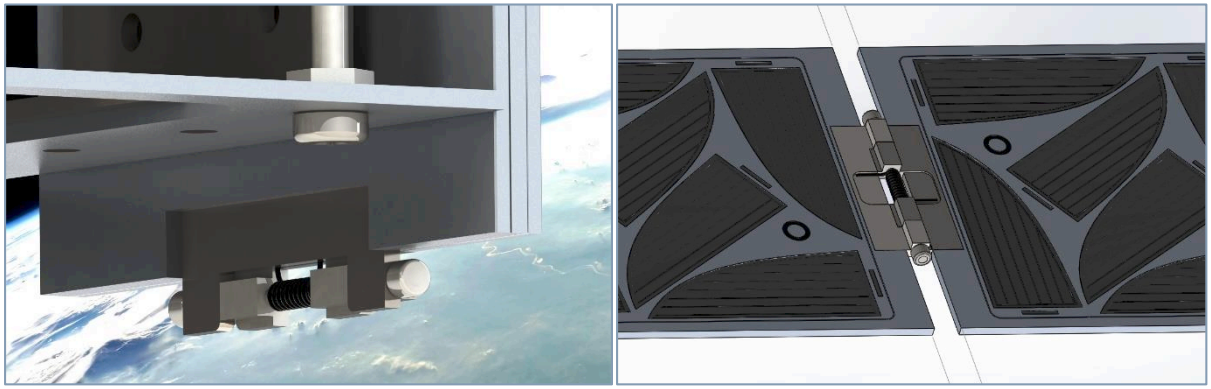

Figure 17. The Thin Spring Hinge at Stowed (left) and Deployed (right) States

The distance between each panel at the same side is 3mm, therefore, the overall length of the two-side solar panels when deployed, is 1111mm.

4.2. Design of Spring-loaded Hinges

4.2.1. The Shaft Spring Hinge

The structure of the customised shaft spring hinge A is shown in **Figure 16**. Setscrew 1: M1.2x2 – fixing the hinge with the hexagonal hollow shaft. Setscrew 2: M1.2x4 – locking the two part of the hinge & acting as the spring hinge shaft. Countersunk head screws 3x2: M1x3 – Fixing the panel 1 with the shaft hinge.

For performance of the spring hinge please refer to Section 5.2. Noting that the hinge parts connecting with panel 1, for left and right side panels, are symmetrical, rather than identical.

4.2.2. The Thin Spring Hinge

The structure of the customised Thin Spring Hinge is shown in **Figure 17**. For performance of the spring hinge please refer to Section 5.2. Unlike the shaft hinge and the panel 1, similar to the panel 2 and panel 3, the Thin Spring Hinges is identical. Therefore, for each system, we need four identical thin spring hinges. Welding will be used for the fixation of the thin spring hinges, as it is the best solution for connecting the stainless steel hinges (1mm thickness) and alloy panels (1mm thickness).

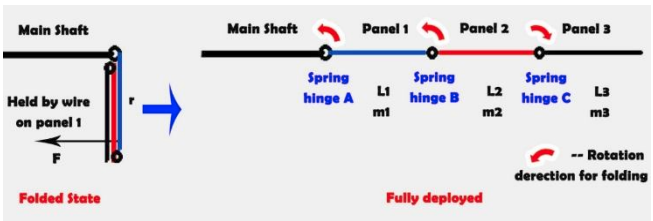

Figure 18. Illustration of Deploying Process

5. Dynamics and Vibration Analysis

5.1. Mechanics Analysis

As shown in the **Figure 18**, when the panels are folded, they will be held by Dyneema wire, and the wire is tired on the burner resistors on the release mechanism PCB. The values and descriptions on the figure are explained in **Table 3**.

"F" is the tensile force of the Dyneema wire that connecting with the burner resistors to held the panels from deploying. Recall from engineering mechanics [24], for statics situation force analysis, only the external forces are considered.

Recall that, $F * r = \boldsymbol{T}_{a0}$

Then we can gain that the tensile force F is:

$$\frac{\boldsymbol{T}_{a0}}{\mathrm{r}} = \frac{0.0117\mathrm{Nm}}{0.115\mathrm{m}} \approx 0.1\mathrm{N}.$$

Applying dynamics analysis for the hinges, the work done by the torque is: $W = \boldsymbol{T} * \varphi$;

Where the φ is the angle that the hinge rotated under the action of torque $\boldsymbol{T}$.

Because we can assume that the torque has a linear relationship with the rotation angel, under the torsion coefficient (spring constant) k, therefore: $\boldsymbol{T}(\varphi) = \mathrm{k} * \varphi$;

Table 3. Value and descriptions of the Symbols

Symbol	Description	Value	Unit
r	Distance between the Main Shaft to the hole to tire Dyneema wire with the burner resistors	115	mm
L1	Distance from the axles of Spring hinge A and Spring hinge B	188.5	mm
L2	Distance from the axles of Spring hinge B and Spring hinge C	171	mm
L3	Distance from the axle of Spring hinge C to the end of Panel 3	171	mm
m1	Mass of the Panel 1 including the mass of the connector to the hinge A and half of hinge B	22	g
m2	Mass of the Panel 2 (including hinge)	19.5	g
m3	Mass of the Panel 3 (including hinge)	18.5	g
$\boldsymbol{\tau}_{a0}$	The torque of spring hinge A (90° Stowed)	19.5	mNm
$\boldsymbol{\tau}_{a1}$	The torque of spring hinge A (Deployed)	7.8	mNm
ka	Spring Constant of hinge A	0.13	mNm/ deg
$\boldsymbol{\tau}_{b0}$	The torque of spring hinge A (180° Stowed)	13.5	mNm
$\boldsymbol{\tau}_{b1}$	The torque of spring hinge B (Deployed)	4.5	mNm
kb	Spring Constant of hinge B	0.05	mNm/ deg
$\boldsymbol{\tau}_{c0}$	The torque of spring hinge C (180° Stowed)	13.5	mNm
$\boldsymbol{\tau}_{c1}$	The torque of spring hinge C (Deployed)	4.5	mNm
kc	Spring Constant of hinge C	0.05	mNm/ deg

At the moment of Stowed situation:

$$\boldsymbol{\tau} = \boldsymbol{\tau}_0, \varphi = \varphi_0;$$

At the moment of deployed situation:

$$\boldsymbol{\tau} = \boldsymbol{\tau}_1, \varphi = \varphi_1;$$

Then the work becomes:

$$W = \int_{\varphi_0}^{\varphi_1} \boldsymbol{\tau}(\varphi) d\,\varphi;$$

$$W = \int_{\varphi_0}^{\varphi_1} k(\varphi_1 - \varphi_0) d\,\varphi = \frac{1}{2} k(\varphi_1 - \varphi_0)^2;$$

Therefore, the elastic potential energy U of corresponding spring hinge is:

$$U = W = \frac{1}{2} k(\Delta\varphi)^2,$$

Where φ_1, φ_0 have to be within the maximum bending angle of the torsion springs.

Noting that,

$$\begin{cases} k_a = 0.13\, mNm/deg = 7.448\, mNm/rad; \\ k_b = k_c = 0.05\, mNm/deg = 2.865\, mNm/rad; \end{cases}$$

There for the elastic potential energy of Panel 1, 2, and 3 becomes:

$$\begin{cases} U_1 = \frac{1}{2} k_a (\frac{\pi}{2})^2 = 0.5 * 7.448 * 10^{-3} * \left(\frac{\pi}{2}\right)^2 = 0.00919J \\ U_2 = \frac{1}{2} k_b (\pi)^2 = 0.5 * 2.865 * 10^{-3} * \pi^2 = 0.0141J \\ U_3 = \frac{1}{2} k_c (\pi)^2 = 0.5 * 2.865 * 10^{-3} * \pi^2 = 0.0141J \end{cases}$$

Therefore, as the rotation direction of hinge B and C are opposite, the overall elastic potential energy is in between U1 and U1+U2+U3:

$$\begin{cases} U_{min} = U_1 = 0.00919J \\ U_{max} = U_1 + U_2 + U_3 = 0.03739J \end{cases}$$

For thin rectangular plate of height *h* and of width *w* and mass *m*, when the axis of rotation parallel to the plate at the short edge,

$$I = \frac{mL^2}{3} [7];$$

When the three panels are fully deployed, its moment of inertia is:

$$I_{max} = \frac{m(L_1 + L_2 + L_3)^2}{3} = \frac{0.06 \times 0.53^2}{3} = 0.00562 \text{kg} \cdot \text{m}^2$$

Recall that angular kinetic energy equation:

$$E_{rotational} = \frac{1}{2} I\omega^2,$$

Assuming that before the moment of the hinge A's impact, the overall elastic potential energy are completely transferred to its angular kinetic energy.

$$U = E_{rotational} = \frac{1}{2} I\omega^2,$$

Combining the above equations,

$$\omega = \sqrt{\frac{2U}{I}},$$

We can gain the range of angular velocity for the impact moment, as shown in the **Table 4**.

Table 4. Range of Angular Velocity $\boldsymbol{\omega}$ for the Impact Moment

$\boldsymbol{\omega}$ $(\boldsymbol{rad/s})$	$\boldsymbol{U_{min} = 0.00919J}$	$\boldsymbol{U_{max} = 0.03739J}$
$I_{max} = 0.00562kg \cdot m^2$	1.808 $\boldsymbol{rad/s}$	3.648 $\boldsymbol{rad/s}$

5.2. Mechanics Analysis

From the above theoretical mechanics analysis, we can gain the range of angular velocity for the impact moment of the custom designed spring hinge A (**Figure 16**). The two spring hinge A are the parts that most likely to be broken during the deployment process. In order to verify its design, we can use the Dynamics Analysis add-on of Solidworks Premium

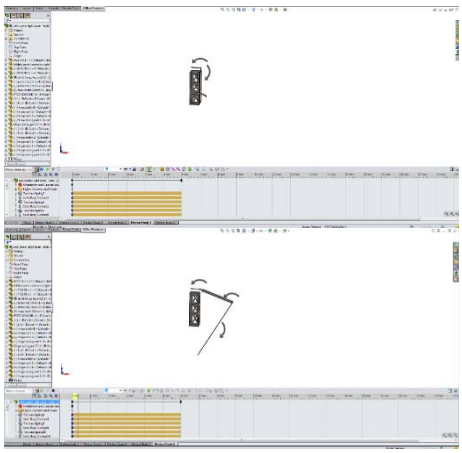

Figure 21. Screenshot of the Dynamics Simulation Process

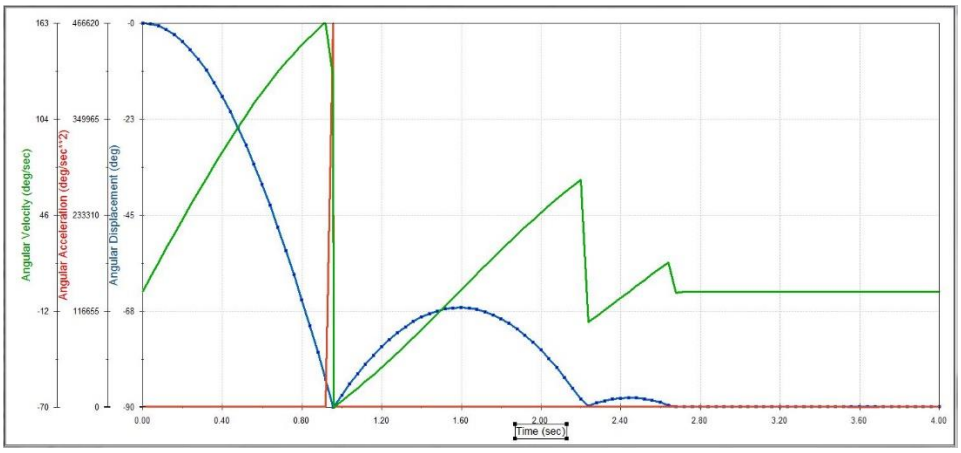

Figure 22. Change of angular velocity, angular acceleration, and angular displacement

software, to simulate the motion data. The above theoretical calculation result can be used for verification.

As shown **Figure 19,** in in order to optimize the calculating speed, all unnecessary parts are removed from the dynamics simulation model. First step is to set the corresponding material properties to the parts that may have impaction with others: AISI 304 stainless steel are set as the material of spring hinges A, B, C; whereas the panels and satellite skeleton are set as 7079 aluminium alloy. **Figure 20** illustrate the process of contact setting between the parts, a 0.2 restitution coefficient, rather than an automatic was set to

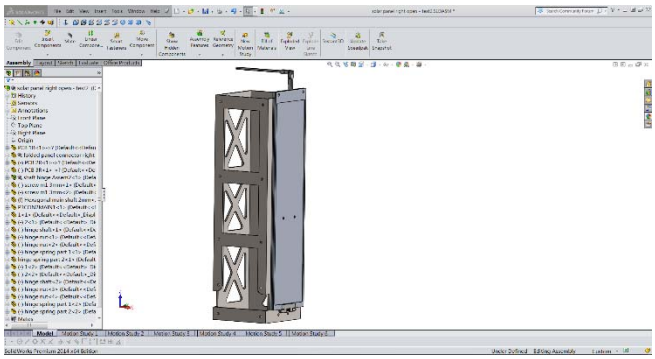

Figure 19. Simplified system model for dynamics analysis (mass of the panels are set as the same)

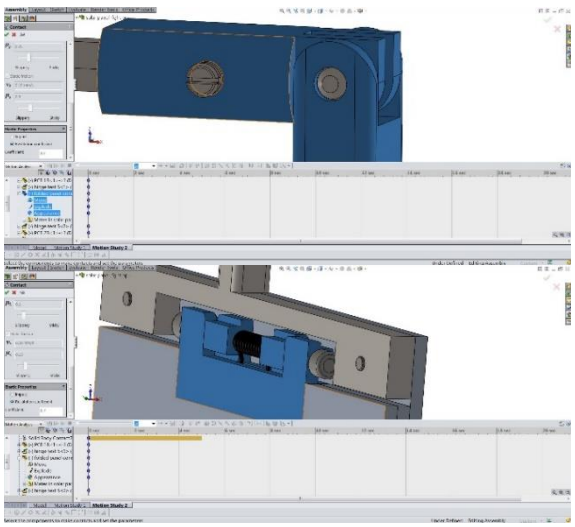

Figure 20. Contact Setting of Spring Hinge A and C

save the calculation time and to make the simulation possible to run without crash. Friction property is also be set to the contact between the satellite skeleton and the panels.

After limit the rotational direction and angle for the three hinges respectively, the corresponding torsional parameters will be set to the software. Noting that before the simulating, the contact surface of different parts (with the contact setting) need to be cut a gap (for example, 0.01mm) to avoid the lock from the software's contact calculation. As shown in **Figure 21,** the dynamics simulation will then be undertaken by Solidwork software's Motion Analysis add-on.

As a result, the simulation data for the deploying process can be output by the software. The change of angular velocity, angular acceleration, and angular displacement are shown in the **Figure 22**.

We can gain that the collision of the hinge A occurs at around 0.9s after release. The angular velocity changes from 163deg/s (anticlockwise, **2.84rad/s**) to -70deg/s (clockwise, **-1.22rad/s**) before and after the impact. At the moment of collision, the instant angular acceleration is 46620 deg/s^2 (**8139rad/s^2**). The minimum distance between the contact surface to the axis of the hinge axle is 1.5mm, whereas the maximum distance is 2.12mm.

Therefore, for the contact surface, the maximum instant liner acceleration for the moment of impact is:

$$a_{max} = \alpha \times r_{max} = 8139\text{rad/s}^2 \times 2.12\text{mm} \times 10^{-3}\text{mm/m} = 17.25\text{m/s}^2$$

For the collision force, recall newton's second law,

$$F_{max} = m \times a_{max} = 0.06\text{kg} * 17.25\ \text{m/s}^2 = 1.035\text{N}$$

The cross area of the contact surface of Hinge A is,

$$S = 1.5\text{mm} * 0.8\text{mm} * 2 = 2.4 * 10^{-6} m^2.$$

Therefore, the collision pressure will not exceed $F_{max}/S = 1.035\text{N}/2.4 * 10^{-6} m^2 = 0.431\text{Mpa}$

By comparing the angular velocity at the moment of collision from the simulation result (**Figure 22**), which is 2.84rad/s, to

the range of angular velocity ω for the impact moment we gained from the mechanics calculation in section 5.1, 1.808 rad/s < ω < 3.648 rad/s (**Table 4**), as the data from theoretical calculation and computational dynamics simulation fit well, the result of the software therefore can also be verified.

For the material of the hinges, we have a selection of 304 stainless steel or the lighter Titanium Ti-6Al-4V (Grade 5) alloy with higher strength. As the Yield Strength of 304 stainless steel is 205Mpa, which is exponentially far higher than 0.431Mpa, we can gain the result that the collision for the hinge A of the deployment process of the solar panels will not lead to structural distortion or notable damage of hinge A. Furthermore, as hinge A is the component that most likely to be broken during the deployment process, the deployment's capability for impact resistance is therefore qualified.

5.3. Vibration Analysis

Abaqus CAE is utilized for the finite element analysis of the vibration test for the panels.

5.3.1. Free Vibration Analysis

As shown in **Figure 23**, in Abaqus CAE, firstly we build trusses and shells to simulate the shaft connecter and three panels respectively. The spring hinges are simplified into five separate rigid connectors.

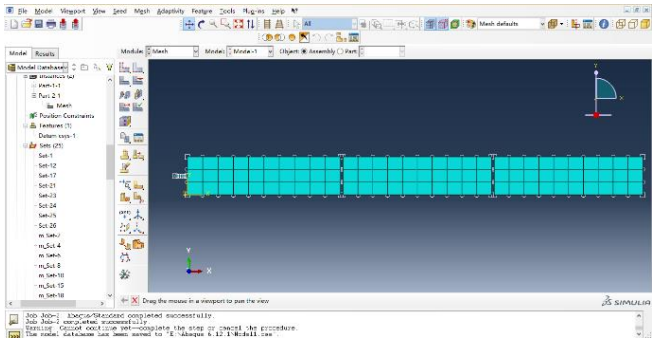

Figure 23. Simplification of the shaft and panels as truss and shell structure in Abaqus

Frame

Index	Description				
0	Increment	0: Base State			
1	Mode	1: Value = 317.47	Freq = 2.8358	(cycles/time)	
2	Mode	2: Value = 11910.	Freq = 17.369	(cycles/time)	
3	Mode	3: Value = 84127.	Freq = 46.162	(cycles/time)	
4	Mode	4: Value = 1.90431E+05	Freq = 69.453	(cycles/time)	
5	Mode	5: Value = 2.25068E+05	Freq = 75.505	(cycles/time)	
6	Mode	6: Value = 4.21591E+05	Freq = 103.34	(cycles/time)	
7	Mode	7: Value = 1.06726E+06	Freq = 164.42	(cycles/time)	
8	Mode	8: Value = 1.72888E+06	Freq = 209.27	(cycles/time)	
9	Mode	9: Value = 2.20463E+06	Freq = 236.31	(cycles/time)	
10	Mode	10: Value = 4.89376E+06	Freq = 352.08	(cycles/time)	
11	Mode	11: Value = 5.44042E+06	Freq = 371.22	(cycles/time)	
12	Mode	12: Value = 7.69556E+06	Freq = 441.51	(cycles/time)	
13	Mode	13: Value = 9.23006E+06	Freq = 483.53	(cycles/time)	
14	Mode	14: Value = 9.81500E+06	Freq = 498.61	(cycles/time)	
15	Mode	15: Value = 1.44894E+07	Freq = 605.82	(cycles/time)	
16	Mode	16: Value = 1.68184E+07	Freq = 652.70	(cycles/time)	
17	Mode	17: Value = 2.63164E+07	Freq = 816.46	(cycles/time)	
18	Mode	18: Value = 2.77954E+07	Freq = 839.09	(cycles/time)	
19	Mode	19: Value = 3.84148E+07	Freq = 986.44	(cycles/time)	
20	Mode	20: Value = 4.09919E+07	Freq = 1019.0	(cycles/time)	
21	Mode	21: Value = 4.37877E+07	Freq = 1053.2	(cycles/time)	
22	Mode	22: Value = 5.44041E+07	Freq = 1173.9	(cycles/time)	
23	Mode	23: Value = 5.79862E+07	Freq = 1211.9	(cycles/time)	

Figure 24. Data of Free Vibration Analysis Result

The properties of 304 grade stainless steel is defined to the hinges and shaft connector, whereas 7079 aluminum alloy (UNS A97079) is defined to panels respectively, followed by assigning the cross section 9 square millimetres to the truss and thickness 1mm to the shell structure respectively.

Boundary condition are applied, and a fixation is added on the root of the truss. For the hinges, only releasing the rotational freedom Rv on the y axis, holding the rotational displacement (Ru, Rw).

In this case, meshing become relatively easy for the shell and truss structure, since the simplification of models are made.

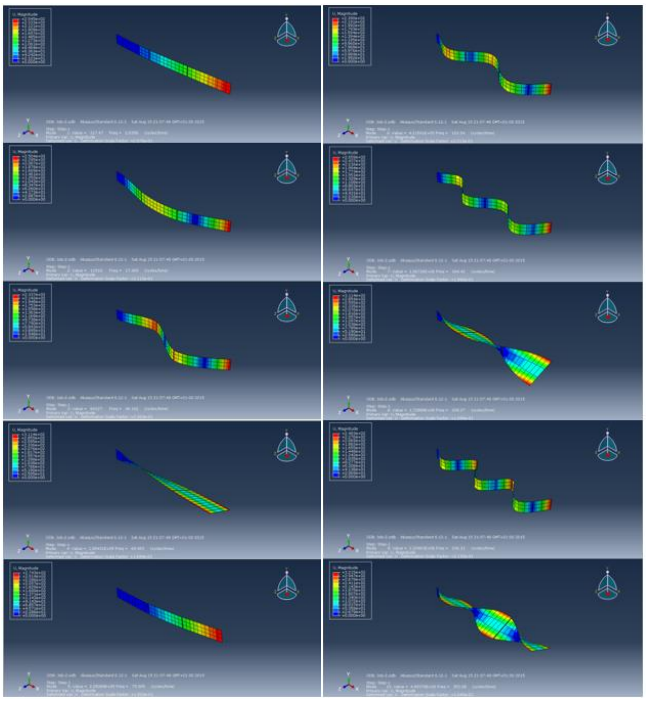

Figure 25. Free Vibration Result Contour Plots

We mesh each panel (shell structure) into 10*3 sections, and the shaft connector (truss structure).

By setting Lanczos as Eigensolver, and valuing 30 as the number of eigenvalues requested, we can began to run the free vibration step (**Figure 24**). We post the response spectrum of the first 10 detected frequencies below, as **Figure 25**.

5.3.2. Forced Vibration Analysis and Response Spectrum

Based on the above-mentioned Abaqus model, by adding a load of 1N to the edge of the panel on the perpendicular direction, we can test the possible vibration response for an acceleration at the deployed situation (**Figure 26**).

As shown in the forced vibration analysis response spectrum by absolute value (**Figure 27**), two large response to the load occur at **17.4 Hz** and **46.2 Hz** (**Figure 28**).

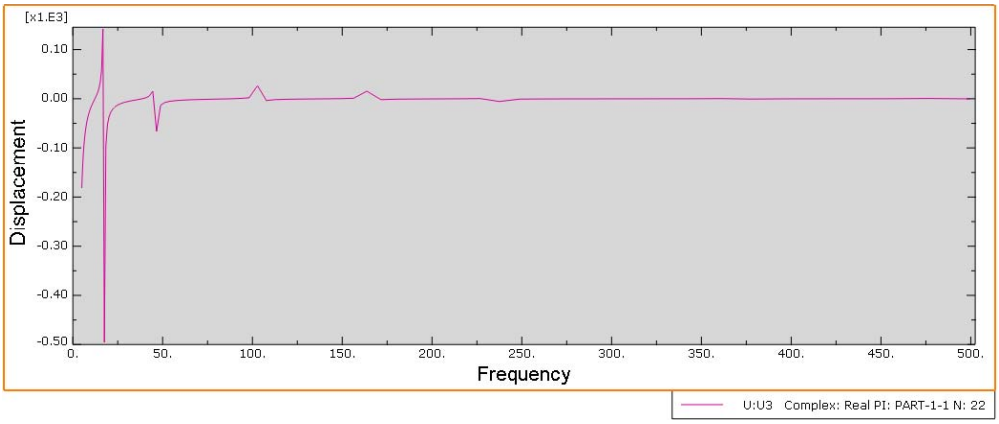

Figure 26. Forced vibration analysis response spectrum (Displacement Magnitude: 10^{-3}Metres)

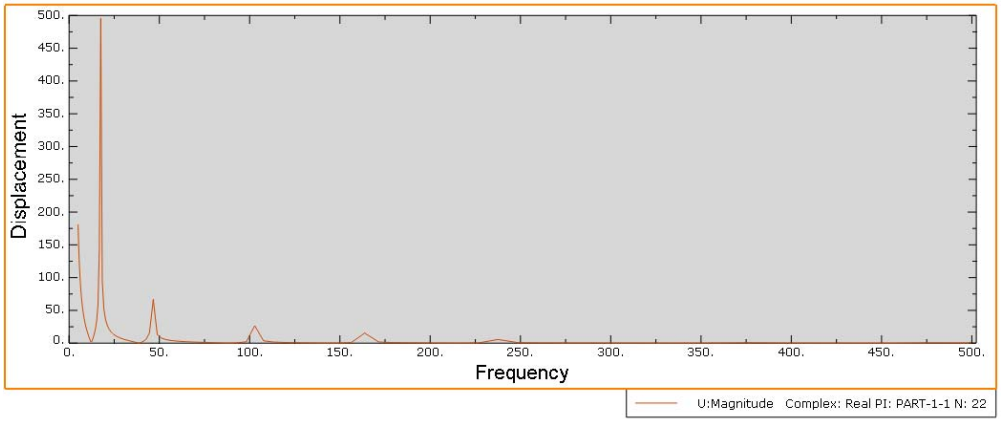

Figure 27. Forced vibration analysis response spectrum by absolute value (Displacement Magnitude: *millimetres*)

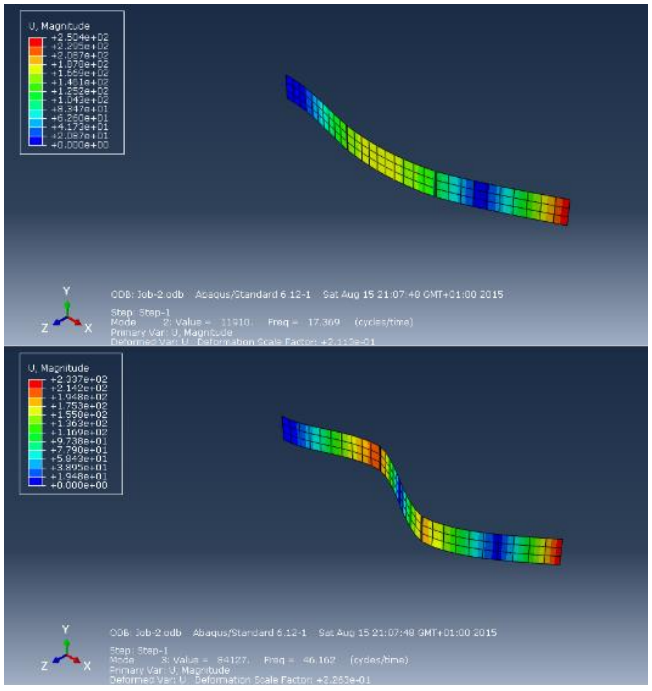

Figure 28. Corresponding Free Vibration Analysis Contour Plots (above: 2nd on 17.4 Hz, below: 3rd on 46.2 Hz)

By comparing the data of the free vibration data (**Figure 24**) we gain earlier, it is easy to find that both of the 17.4 Hz and 46.2 Hz are matched, as the first and second bending mode, so we can now see that this two modes are easily excited.

Therefore, we should have to aware these two vibration frequency regions around 17.4 Hz and 46.2 Hz as such vibrational load applied to the panels could excite a large-amplitude vibration, and may lead to failures.

Furthermore, except the most notable and dangerous 17 Hz and 46 Hz regions, as shown in **Figure 27**, the vibration frequency ranges around 103 Hz, 164 Hz, and 236 Hz should also be avoid as much as possible.

6. PROTOTYPING AND SUGGESTIONS

6.1. 3D Printing Parts

For the internal gear structure (**Figure 29**), high resolution plastic 3D printing is a better manufacturing option than the aluminium alloy CNC processing for formal production.

Figure 29. The CAD Design of the Internal Gear Structure and Its Assembly

Firstly, Additive manufacturing enable designs to acquire demanded strength with a lighter but more complicated structure. By using light material such as the photosensitive

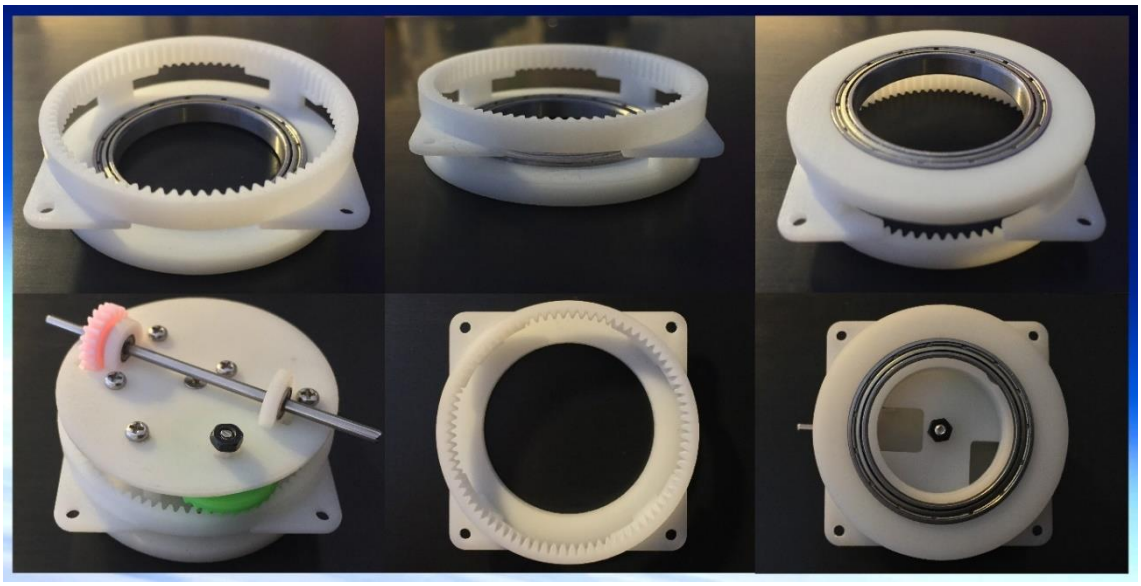

Figure 30. The detail view of Stereolithography 3D printed internal gear structure and its assembly

resin plastic, the effect will be more than doubled. The internal gear structure's volume (3805.48 cubic millimetres) is notable higher than the thin-panel structures, such as the top board, so it is better to reduce its weight by 3D printing; As a result, the mass of the internal gear's resin version is only 3.88 grams, whereas that of the aluminium alloy version is 10.45 grams.

Secondly, the utilisation of Additive Manufacturing significantly reduced the cost for building complicated structures. In this case, the manufacturing price of 3D printing is significant less than that of CNC processing. For the 3D printed internal gear structure (**Figure 30**), the cost of it is less than £2 each from the supplier we chose. In contrast, for the metal CNC processing, £27.06 is needed for only a standard 80 tooth 0.5 mod internal gear from an UK supplier. And we need customization such as skiving the outer surface of the ring, and holes drilling for fixation. The price for the metal CNC processing will be imaginably higher than £50 for each of the internal gear structure.

Figure 31. Comparison of the CNC (left) and 3D printing (right) solutions for Gearbox structure

Figure 32. Two structure parts that can take advantage of using 3D printing for production

Finally, for the internal gear structure, 3D printing's resolution is enough for the requirement. As a matter of fact, the quality of the internal gear structure shows that photosensitive resin 3D printing technology's resolution is far better than our initial expectation. As shown in **Figure 30**, the photosensitive resin 3D printing's resolution is high enough for the 0.5 mod gear; the gear matches smoothly, although from the beginning we just order its 3D printing as a concession to the limited budget. On the other hand, for the parts without thin-panel structure, there is no distortion can be found on them, as the thin-panel structures may lead to unwanted distortion.

Another example for the advantage of 3D printing can be shown in **Figure 31**. 3D printing enable complicated design to be easily manufacturable. Therefore, relatively complicated design (an integration from three separate parts into one strengthened integral part) can be utilized to make the gearbox be more compact (1mm less thickness compare to the CNC processing version), and more stable.

Furthermore, the prototyping also proves that the Modulus 0.5 gear can be 3D printed by high resolution (Stereolithography technology, SLA) photosensitive resin 3D printing (**Figure 30**), and therefore we can print the customised gear (the green gear in **Figure 10**) in our design to further save the cost, as the budget spend on two custom gears (£15 each) is in fact higher than that of the 3D printed 18 parts (£24.5 in total). For those semi-customized (cut to required thin thickness for the limited space of the gearbox) copper pinion gears, since the cost (£1.5 each) is not much, considering the tooth number of them are only 8 and 10, it's better to use the metal gears for guaranteeing the transmission performance.

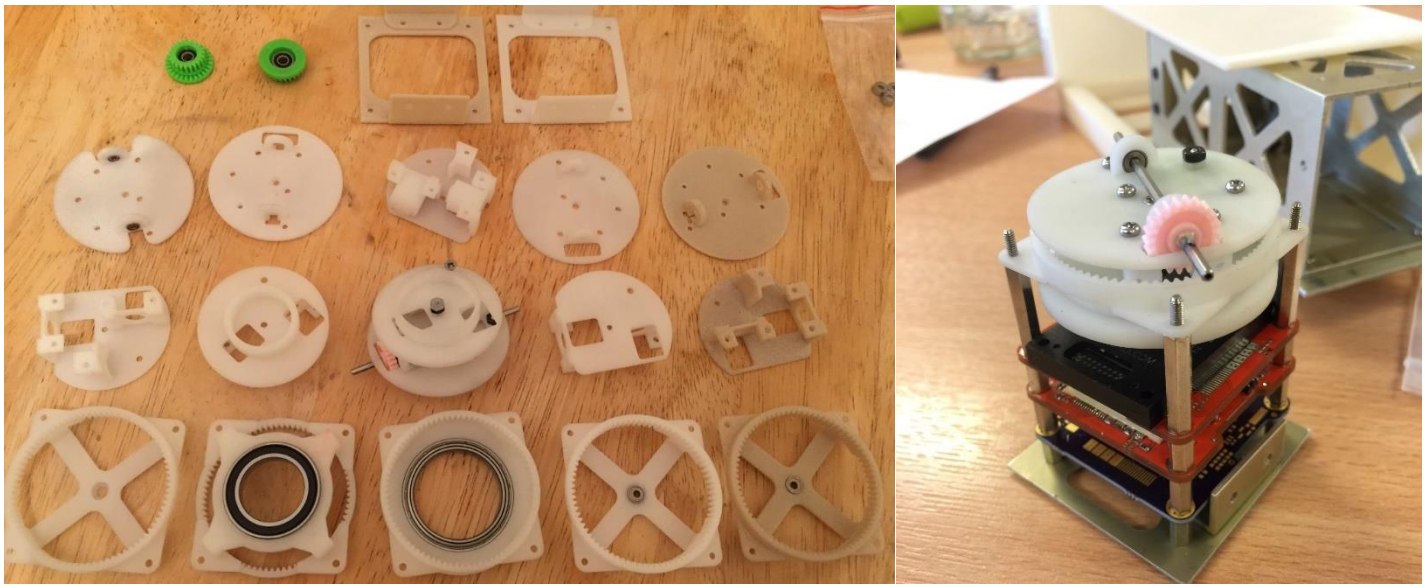

Figure 33. Left: Parts for the gimbal prototyping; Right: Mounting the gimbal with PCBs and threaded rods

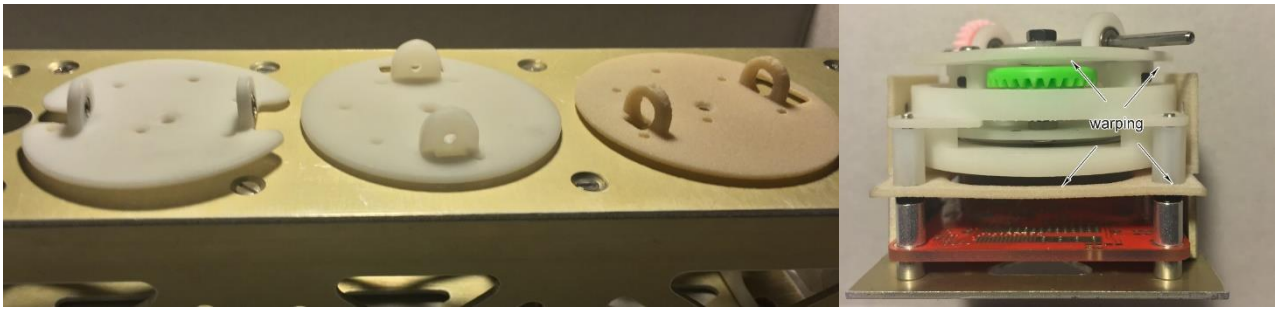

Figure 34. Unwanted warping is a common problem of 3D printing parts with thin-panel structure

In conclusion, by integrating the cost, qualities, mass, and mechanical property into account, we suggest to use Stereolithography 3D printing (SLA) technologies (photosensitive resin material, minimum resolution 100 micrometres) to manufacture the internal gear structure part (**Figure 32 left**), gearbox structure part (**Figure 32 right**), and the 0.5 Modulus customized double crown-spur gear.

6.2. Parts Suit for CNC Processing Production

For the parts that must use metal materials, such as the spring hinges, it is better to choose conventional CNC processing to manufacture. Which is partly because of that, although there are many commercial metal 3D printing suppliers, the price of metal 3d printing is even higher than CNC processing, and the precision of commercial metal 3D printing is about 100 micrometres, which is much worse than that of conventional machining.

Furthermore, for the customised parts that we have to use metal, neither very complicated structure, nor cemented carbides that difficult to machining, such as titanium alloy, are necessary to apply. That is to say, in this project, for customised metal component, CNC machining is the preferred choice rather than metal 3D printing.

As shown in **Figure 33**, we ordered 3D printing parts with different processing methods, although not each parts of them are perfectly suit for 3D printing. Thin-panel structures may lead to unwanted warping and distortion [25]. For Stereolithography rapid prototyping technology (SLA), due to the fast reaction, together with the almost unavoidable cure shrinkage and some effects caused by thermal factors, which inducing stress in the manufacturing components built up from layer to layer, will lead to notable warping and curl phenomenon [26].

As shown in **Figure 34**, warping phenomenon can be seen easily on all of the parts manufactured by Stereolithography (SLA) technology with photosensitive resin material (left two in write) and the part built by Selective Laser Sintering (SLS) technology with nylon material (right one in yellow), although less warping can be seen on the middle one and right one with an appropriate symmetrical round design. On the other side, for the two parts we suggest to use 3D printing (**Figure 32**), without thin-panel structure, there is no distortion can be found on them.

In conclusion, by integrating the cost, qualities, mass, and mechanical property into account, we suggest to use conventional CNC machining to manufacture the customised spring hinges, the top board (**Figure 34 Left**), stand board (**Figure 34 Right**), and other customised parts with large-sized thin-panel structures.

6.3. Suggestions for Further Work

One suggestion is about the gear teeth number, all of the teeth number we selected is even number, as the gear set is the best combination based on the available gears in the market. However, it is possible to choose gears with odd number teeth, by doing this we can distribute the potential gear wear among all gear teeth uniformly, rather than repeating the wear by a potential incorrect profile rapidly from each rotation.

Another suggestion for PocketQube Satellite is to reduce the thickness of the skeleton from 1.5mm to 1mm. By doing this on the alloy 3P skeleton, at least 28.22 grams can be saved from the 151 grams net weight, which means 18.6% of the skeleton's mass can be cut off easily. Since no strong strength will forced on the skeleton directly throughout the satellite's life span, it will make no different to its mechanical performance yet reducing its weight, saving the propellant and launching cost.

What's more, other suggestions for the further work are:

• The control PCB for stepper motors have to be built and tested. One suggestion is integrating the controller of both the two motors on the same PCB, which can further save the limited onboard space.

• A lock mechanism may be further designed, to dent and then lock the spring hinges after the deployment, to reduce the shake generated by the hinge impact.

• The four compression springs on the threaded rod need to be freely mounted on sleeves, or changing the threaded rod to smooth rod for this area, as the prototype shows that the springs may be blocked by the thread.

• Further designing a deployable antenna system on same gimbal as there are still reserved for further add-ons, and the antennas can use the same release board with the solar panel subsystem, for their deployment. The solar panel have a deployed length of 0.53m each side, antennas could also be tried to attached with the solar panels, which not only allowing the designer to add a long antenna, will also allowing these antennas to be pointed any direction omnidirectionally.

7. SUMMARY

In this work we put forward a solution for developing a commercial valid solar panel deployment and tracking system for PocketQube pico-satellite. During the designing and keep optimizing process, a gearbox structure is designed to compact the gimbal system greatly, by using a planetary double crown-spur gear meshing with a ring-type internal gear, enabling to install two micro stepper motors parallel to the rotating gimbal. Followed by that, a further optimizing is undertook, for stabling the rotation to reduce vibration, while simultaneously enabling an easier arrangement of the wires. Trade-off analysis is done to meet the balance of low weight, larger panel dimension, and higher efficiency, moreover, reliability, manufacturability, and cost are considered from the beginning, as commercial production and launch is expected after the project.

During the prototyping phase, full scale prototypes of the gimbal subsystem was built to verify the design and to compare different design details. By using different rapid prototyping technologies and materials, and comparing different designs, the most feasible solution, as well as the suggestions for the future development, were put forward.

On the other hand, two versions of the gimbal subsystem are designed and compared with different manufacturing processes and materials: 3D printing plastic version, and CNC processing aluminum alloy version. A discussion is focus on the selection of processing for various parts. Meanwhile, discussions about some other problems are also put forward.

After the whole process from design to optimization, from analysis to prototyping, and from discussion to suggestion, it is obvious to say that further work, especially those we mentioned in the suggestion part, are very necessary to make the project more complete.

REFERENCES

[1] E. Buchen and D. DePasquale, "2014 Nano/Microsatellite Market Assessment," Space Works Enterprises, Inc. (SEI), 2014.

[2] S. R. Tsitas and J. Kingston, "6U CubeSat commercial applications," *Aeronautical Journal,* vol. 116(1176), pp. 189-198, 2012.

[3] P. Harkness, M. McRobb, P. Lützkendorf, R. Milligan, A. Feeney and C. Clark, "Development status of AEOLDOS - a deorbit module for small satellites. Advances in Space," *Advances in Space,* vol. 54 (1), pp. 82-91., 2014.

[4] L. Dudas, L. Szucs and A. Gschwindt, "The spectrum monitoring system by Smog-1 satellite," in *2015 Conference on Microwave Techniques, IEEE*, 2015.

[5] NASA, "NanoRacks-LitSat-1," [Online]. Available: http://www.nasa.gov/mission_pages/station/research/experiments/1642.html. [Accessed Jul 2016].

[6] POCKETQUBE SHOP, "How much does a PocketQube Cost?," [Online]. Available: http://www.pocketqubeshop.com/cost/. [Accessed Aug 2015].

[7] R. A. Serway, Physics for Scientists and Engineers, 2nd Ed., Saunders College Publishing, 1986.

[8] FAULHABER, "Brushless DC-Servomotors 0824," [Online]. Available: https://fmcc.faulhaber.com/details/overview/PGR_18902_13822/PGR_13822_13814/en/GLOBAL/. [Accessed Aug 2015].

[9] Nanotec, “Sensorless control of stepper motors,” [Online]. Available: http://en.nanotec.com/support/application-notes/sensorless-control-of-stepper-motors/. [Accessed Aug 2015].

[10] Nanotec, “SP1018M0204-A Permanent Magnet Stepper Motor,” [Online]. Available: http://en.nanotec.com/products/169-sp10-sp55-permanent-magnet-stepper-motors/. [Accessed Aug 2015].

[11] Canon, “USM lens technology: magic motors,” [Online]. Available: http://cpn.canon-europe.com/content/education/technical/usmlens_technology.do. [Accessed Aug 2015].

[12] P. Toscani, “The piezoelectric motor with progressive wave.,” [Online]. Available: http://www.pierretoscani.com/echo_shortpres.html. [Accessed Sep 2016].

[13] Piezomotor, “Rotary Piezoceramics Motors,” [Online]. Available: http://www.piezomotor.com/. [Accessed Aug 2015].

[14] Transusm, “Transusm ultrasonic motor (in Chinese language),” [Online]. Available: http://www.transusm.com/. [Accessed Aug 2016].

[15] PI, “PI (Piezo Technology),” [Online]. Available: http://www.piceramic.com/. [Accessed Aug 2016].

[16] MICROMO, “FAULHABER FDM0620 Series,” [Online]. Available: http://www.micromo.com/catalog/category/view/s/fdm0620/id/121?limit=40. [Accessed Jul 2016].

[17] MICROMO, “Stepper Motor Datasheets - PRECIstep Technology,” [Online]. Available: http://www.micromo.com/products/stepper-motors/stepper-motors-datasheets. [Accessed Jul 2015].

[18] Portescap, “P010 064 Disc Magnet High Speed Step Motor,” [Online]. Available: http://www.portescap.com/products/disc-magnet-motors/p010-064-disc-magnet-high-speed-step-motor. [Accessed Aug 2015].

[19] Portescap, “P010 104 Disc Magnet High Speed Step Motor,” [Online]. Available: http://www.portescap.com/products/disc-magnet-motors/p010-104-disc-magnet-high-speed-step-motor. [Accessed Aug 2015].

[20] Nanotec, “Custom-Made Design,” [Online]. Available: http://en.nanotec.com/products/customer-specific-solutions/custom-motors/custom-made-design/. [Accessed Aug 2015].

[21] J. S. Rao, Kinematics of machinery through hyperworks (Vol. 18), Springer Science & Business Media, 2011.

[22] Micromo, “White Paper - Microstepping: Myths and Realities,” [Online]. Available: http://www.micromo.com/media/wysiwyg/Technical-library/Stepper/6_Microstepping%20WP.pdf. [Accessed Aug 2015].

[23] TrisolX, “TrisolX-Solar-Wing-Data-Sheet,” [Online]. Available: www.trisolx.com. [Accessed Jun 2016].

[24] R. C. Hibbeler, Engineering mechanics. Statics and dynamics, 13th Ed., Pearson, 2013.

[25] W. Zhao, D. Li and B. Lu, “Investigation of the Part Deformation in Stereolithography,” *Journal of Xi'an Jiaotong University,* vol. 07, 2001.

[26] M. Hofmann, “3D printing gets a boost and opportunities with polymer materials,” *ACS Macro Letters,* vol. 3(4), pp. 382-386, 2014.

BIOGRAPHY

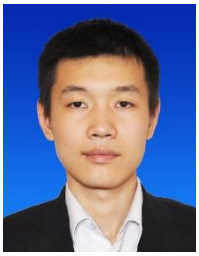

Daizong Li *received a B.Eng. in Aerospace Manufacturing Engineering from Nanchang Hangkong University in 2012, and an MSc in Aerospace Engineering and Management from University of Glasgow in 2015. He then become a project manager of the C919 Aircraft Project Management Office, COMAC Shanghai Aircraft Customer Service Co Ltd, Commercial Aircraft Corporation of China, since 2016. Prior to COMAC, he has interned in AVIC CSC, Airbus China, and Alba Orbital.*

Tom Walkinshaw *is a Scottish entrepreneur. He is the founder and CEO of Alba Orbital Limited (PocketQube Shop), a Kickstarter-funded company specializing in the production of PocketQubes. Alba's first satellite, Unicorn-1, was built for the European Space Agency. The satellite is a 2p (double PocketQube) and will trial the world's first Leo-Geo intersatellite link on a Picosat with Avanti Plc. Alba Orbital was featured in CNN's 2015 top 10 start-ups to watch. Tom holds a degree in Business from Glasgow Caledonian University.*

Patrick Harkness *obtained a MEng degree in Aeronautical Engineering from The Queen's University of Belfast in 2003 and a PhD in space debris mitigation from Cranfield University in 2007. He then worked with Lockheed Martin on the subject of magnetohydrodynamic flow control before taking up a postdoctoral role at the University of Glasgow, focusing on ultrasonics, in 2008. In 2014, he became a senior lecturer in Space Systems Engineering. Patrick's main researches are in space deployable structures, and planetary surface exploration tools.*